New processing routes for Zr-based ODS ferritic steels

Oñoro, M.; Salas-Colera, E.; Parnell, S.R.; Martin-Diaconesu, V.; Alba Venero, D.; Leguey, T.; de Castro, V.; Auger, M. A.

DOI
10.1016/j.nme.2024.101713

Publication date
2024

Document Version
Final published version

Published in
Nuclear Materials and Energy

Citation (APA)
Oñoro, M., Salas-Colera, E., Parnell, S. R., Martin-Diaconesu, V., Alba Venero, D., Leguey, T., de Castro, V., & Auger, M. A. (2024). New processing routes for Zr-based ODS ferritic steels. *Nuclear Materials and Energy*, *40*, Article 101713. https://doi.org/10.1016/j.nme.2024.101713

Nuclear Materials and Energy 40 (2024) 101713

Contents lists available at ScienceDirect

Nuclear Materials and Energy

journal homepage: www.elsevier.com/locate/nme

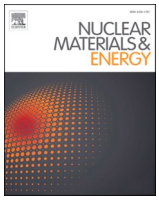

New processing routes for Zr-based ODS ferritic steels

M. Oñoro [a,*], E. Salas-Colera [a], S.R. Parnell [b], V. Martin-Diaconesu [c], D. Alba Venero [d], T. Leguey [a], V. de Castro [a], M.A. Auger [a]

[a] Department of Physics, Universidad Carlos III de Madrid, Avenida Universidad 30, 28911 Leganés, Madrid, Spain
[b] Faculty of Applied Sciences, Delft University of Technology, Mekelweg 15, 2629 JB Delft, The Netherlands
[c] ALBA Synchrotron – CELLS, Carrer de la Llum 2-26, 08290 Cerdanyola del Vallès, Barcelona, Spain
[d] ISIS Neutron and Muon Facility, Rutherford Appleton Laboratory, Didcot OX11 0QX, United Kingdom

ARTICLE INFO

Keywords:
ODS steel
Zr
STARS
Nanoparticles
SANS
XAS

ABSTRACT

In this work, Zr addition is proposed to refine the nanoparticle dispersion in an ODS RAF steel of composition Fe-14Cr-2W-0.3Zr-0.24Y (wt.%). Three batches of material are obtained using pre-alloyed atomized powder, where yttrium is directly introduced in the melt, and manufactured through three different processing routes. First route is based on the newly developed STARS route that aims to avoid subsequent mechanical alloying. The second route explores the impact of mechanical alloying in pre-oxidized powders. The third route uses mechanically alloyed powders without the pre-oxidation process. The ODS-powders were individually consolidated by hot isostatic pressing and later hot rolled. The obtained materials were characterized by small-angle neutron scattering (SANS) and X-ray absorption spectroscopy (XAS) techniques. SANS and XAS analysis point out the absence of oxide nanoparticles in the material based on the STAR route. SANS analysis confirms that the mechanically alloyed materials do exhibit the presence of nanoparticles. These are identified as Zr-O-rich nanoprecipitates by XAS and the calculated A-ratio by SANS is linked with the phase $Y_2Zr_2O_7$. Their radii are in the range of 3–3.6 nm. XAS results show that mechanical alloying minimizes the initial differences regarding the oxidation state between the ODS powders with and without pre-oxidation.

1. Introduction

Nuclear fusion reactors represent a worldwide technology challenge in both research and industrial development. One related leading topic is structural materials design and production [1–3]. Particularly, oxide dispersion strengthened (ODS) reduced activated ferritic (RAF) steels are considered one of the most advanced materials candidates in fusion reactor applications [4–6]. They are characterized by superior mechanical strength at high temperatures and radiation damage resistance, supported by fine grain sizes, formation of secondary phases and high dislocation densities and a homogeneous distribution of nanosized Y-rich oxide particles [7,8]. Moreover, the nanosized oxide particles may act as sinks for radiation defects, hence increasing the irradiation resistance of the material [9,10].

The mechanical properties of ODS steels reveal exceptional performance, primarily due to the presence of uniformly distributed nanosized oxide particles within the steel matrix [11]. These nanoparticles enhance the mechanical response through several mechanisms: they impede dislocation motion, significantly increasing yield strength and tensile strength even at elevated temperatures; the fine dispersion of oxide particles within the matrix contributes to grain refinement, particularly in ODS RAF steels, which further improves strength and toughness by restricting grain boundary movement during deformation; additionally, these nanoparticles act as pinning points that stabilize the microstructure against grain growth at high temperatures, maintaining the fine grained structure necessary for high-temperature strength.

From the perspective of radiation resistance, the nanoparticles play a crucial role in mitigating the detrimental effects of radiation, which, in steels can induce the formation of voids, dislocation loops, and other defects that can ultimately degrade their mechanical properties [12]. The finely dispersed oxide particles in ODS steels serve as effective sinks for these radiation-induced defects. By capturing and annihilating vacancies and interstitials, the nanoparticles reduce the accumulation of radiation damage within the steel matrix, thus preserving its structural integrity under prolonged exposure to high neutron fluxes. This unique ability not only enhances the radiation tolerance but also prolongs the

* Corresponding author.
E-mail address: monoro@fis.uc3m.es (M. Oñoro).

https://doi.org/10.1016/j.nme.2024.101713
Received 16 February 2024; Received in revised form 9 June 2024; Accepted 16 July 2024
Available online 17 July 2024

service life of ODS steels in the harsh environment of nuclear reactors, making them promising candidates for structural applications in fusion technology [9].

ODS RAF steels are based on an Fe-Cr matrix, with Cr content between 12–16 wt.%, and the addition of other low-activation metallic elements. Zirconium and/or titanium would enhance the precipitation and refinement of the oxide nanoparticles for improving strengthening and radiation resistance of the material [13–15]. Titanium is known as a key element to favor the refinement and homogeneous distribution of Y-rich nanoprecipitates in ODS steels [9,16]. Titanium substitution by zirconium may promote an even finer nanoparticle dispersion [17], due to the higher stability of Y-rich nanodispersoids by the higher binding energy of zirconium in a Fe-matrix. The selection of zirconium will also imply a cost reduction in the production of ODS steels at laboratory and industrial scales, since zirconium is significantly cheaper than titanium [18,19]. The experimental data available on Zr-based ODS steels is still scarce [15,17,20]; this work aims to contribute to increase the current knowledge for this ODS RAF steels variant. Most investigations addressing the production of ODS steels with zirconium or other chemical alternatives focus on the substitution of yttrium by zirconium [21], which is not the presented approach; those investigations postulate alternative oxides (as for example ZrO_2) based on their Gibbs free enthalpies and thermal stabilities and have already confirmed the potential of these candidates to produce ODS RAF steels.

The STARS route introduces yttrium directly in the melt prior to gas atomization with Ar and bypasses the mechanical alloying step. However, inert gas atomization minimizes the necessary oxygen gain to later form nanometric oxides. The STARS route is designed to introduce the necessary oxygen content by surface oxidation of the prealloyed metallic atomized powder [22]. This oxidation forms a thin oxide layer on the powder particle surfaces that will later dissociate during high temperature consolidation. Then, the oxygen will diffuse and reach the yttrium and zirconium atoms to form Y-rich or Y-Zr-rich nanodispersoids. Oxygen intake in this powder is additionally explored by the traditional step of mechanical alloying, on powders with and without previous surface oxidation. This research aims to present novel work on the comparison of ODS steels produced by using or avoiding the mechanical alloying step and analyzing their impact on the precipitation and refinement of the expected nanodispersion of oxide particles.

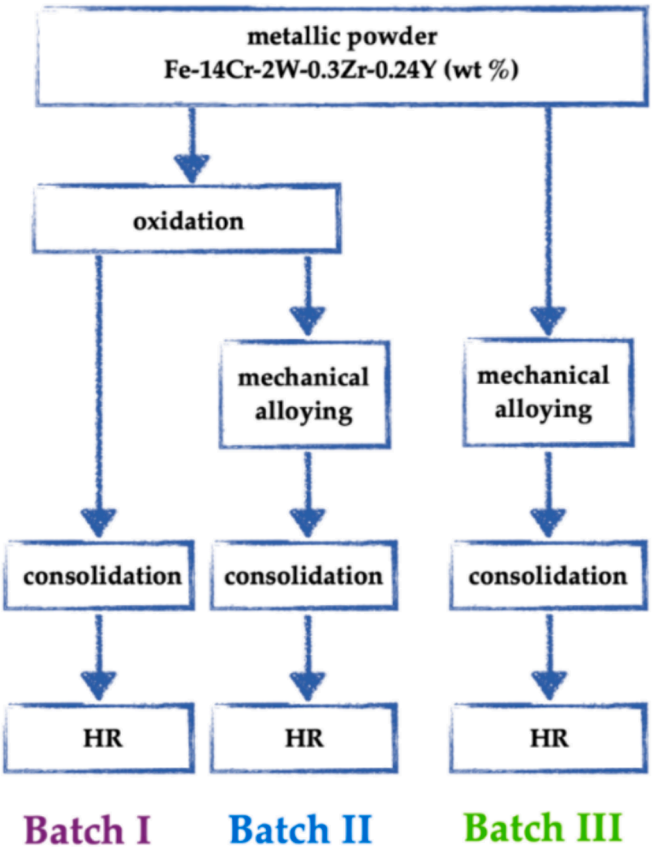

Fig. 1. Schematic of the production routes to manufacture three batches of Zr-based ODS steels.

Previous studies have focused on studying the stability of an ODS RAF steel with chemical composition Fe-14Cr-2W-0.4Ti-0.3Y_2O_3 (wt.%) at fusion power reactors relevant operational conditions [23–25]. Benefiting from the knowledge acquired, the design, production and characterization of a new ODS RAF steel variant is being addressed. The chemical composition of the new proposed material is defined by: (a) Substitution of the 0.4 wt% Ti in the mentioned composition by 0.3 wt% Zr to potentially enhance the nanoparticle precipitation and size refinement; and (b) Addition of 0.24 wt.% Y in the melt prior to atomization as a nanoparticle precursor, instead of 0.3 wt.% Y_2O_3 nanosized powder typically added in the mechanical alloying step. The new nominal chemical composition is Fe-14Cr-2W-0.3Zr-0.24Y (wt.%).

Three processing routes were investigated (Fig. 1). Two of them include mechanical alloying and the other one explores the STARS route, which avoids mechanical alloying. Powders obtained by each route, referred as Batch-I, Bach-II and Batch-III, were individually consolidated by hot isostatic pressure (HIP) followed by hot rolling (HR). The aim of this work is to present the design and production of a Zr-based ODS steel and the initial characterization of the nanoparticle dispersion by small angle neutron scattering (SANS) and X-ray absorption spectroscopy (XAS) techniques.

2. Experimental

2.1. Processing route

The processing route followed to manufacture the Zr-based ODS steel is described as follows:

1. Yttrium was included in the melt to obtain prealloyed Fe-Cr-W-Zr-Y gas atomized powder. The metallic Fe-14Cr-2W-0.3Zr-0.24Y (wt.%) powder was atomized with argon gas of high purity. It was sieved to obtain particles below 500 μm in size. A total amount of 3 kg of powder was produced and provided by CEIT-BRTA: 2 kg were surface oxidated and 1 kg was not. The oxidized powder was subdivided into two different sets, of 1 kg each. First set of 1 kg was directly consolidated with no mechanical alloying (Batch-I in Fig. 1). The second set of 1 kg and the 1 kg of non-oxidized original powder were mechanically alloyed individually and later consolidated (Batch-II and Batch-III, respectively, in Fig. 1)
   Oxidation was promoted through a thermal treatment below 723 K under an oxidizing atmosphere that leads to logarithmic oxidation kinetics, allowing a fine control of the oxygen intake [26] up to a 1540 ppm O_2 content. Chemical composition of the obtained powders was performed by inductively coupled plasma mass spectrometry (ICP-MS) and the oxygen content was determined by the fusion method under inert gas. A detailed chemical composition is summarized in Table 1. It is worth noting the difference in O_2 content between the original and oxidized atomized powders and the influence of ball milling, that minimizes this difference, but different N contents could be appreciated.
2. Mechanical alloying was performed in a planetary mill with austenitic steel vessels and balls under an Ar atmosphere at 300 rpm maximum rotational speed. The ball-to-powder ratio was 10:1 and the total milling time 27 h. The mill performed four 2 h cycles, alternated with 15 min pauses for cooling; the Ar atmosphere was renewed at intervals of 9 h

Table 1
Chemical composition for the Zr-based ODS steels at different stages of its processing route in wt.% (MA stands for mechanically alloying and n.m. for not measured elements).

Element	Original powder	Oxidized powder (Batch-I)	Oxidized powder + MA (Batch-II)	Original powder + MA (Batch-III)
Fe	Bal.	Bal.	Bal.	Bal.
Cr	13.73	13.73	13.00	13.00
W	1.89	1.89	1.80	1.90
Zr	0.32	0.32	0.31	0.31
Y	0.26	0.26	0.23	0.23
O	230 ppm	1540 ppm	0.33	0.29
C	n.m.	n.m.	0.11	0.11
N	n.m.	n.m.	0.23	0.37
Al	n.m.	n.m.	<0.005	<0.05
Si	n.m.	n.m.	<0.05	<0.05
S	n.m.	n.m.	0.008	0.008

3. Consolidation. HIP was used to individually consolidate the three batches of material. The consolidation process of the three powder batches was performed by CEIT-BRTA using their own-designed (low carbon steel) cans with an approximate size of 40 × 40 × 80 mm^3. The mechanically alloyed powders were sieved to discard agglomerated particles over ~500 μm. Then, the cans were filled, vacuum degassed and sealed prior consolidation in an Ar pressure of 150 MPa at 1373 K for 3 h. Heating rate was set to 10 K/min; the consolidated batches were air cooled at ambient conditions
4. After HIP, the three cans were hot rolled. HR was performed at the OCAS Zwijnaarde Center in Belgium. The capsules were preheated at 1373 K for 30 min and rolled for 15 passes, achieving an approximate final thickness of 10 mm (~75 % thickness reduction). Between 5 and 12% rolling reductions were induced per pass and intermediate reheating was performed once. The reheating time was 15 min
Hot rolling of Batch-I was successful, since no edge cracks were observed. After the 9th pass the material was reheated for 15 min. Final thickness for Batch-I was 9.4 mm. Batch-II was rolled in an identical manner as Batch-I; minor edge cracks formed but, overall, the rolling of Batch-II was successful as well. Final thickness for Batch-II was 9.7 mm. For Batch-III, it was attempted to avoid the intermediate reheating step. Significant edge crack formation occurred after the 12th pass, at a thickness around 16 mm. To compare the microstructure of the three batches, the rolling process continued to the final thickness target of 10 mm. The formed cracks continued to develop. The cracks were mainly placed on one side of the plate. Final thickness for Batch-III was 10.0 mm. Overall, the flatness of all capsules was good.

2.4. Characterization techniques

The crystallographic phases present in the material were characterized by X-ray diffraction. These measurements were performed at Universidad Carlos III de Madrid facilities, in a X-Pert Phillips diffractometer using Cu radiation at 40 kV, 40 mA, 0.04° step width and 2.5 s measuring time per step; and at the Materials Science and Engineering Department at Delft University of Technology, using a Bruker-AXS D8 diffractometer in Bragg-Brentano geometry, with Cu K_α radiation at 45 kV and 40 mA, 0.015° step size in 2θ and 2 s as measuring time per step.

Small-angle neutron scattering (SANS) and x-ray absorption spectroscopy (XAS) are advanced characterization techniques, which, in this work, have been used to characterize the dispersion of nanoparticles in oxide dispersion-strengthened (ODS) steels on a macroscopic scale. These techniques enable the analysis of large material sections (0.1–1 cm^2). The size distribution of nanoscale phases can be measured by SANS, while chemical characterization can be performed by XAS.

XAS is divided into two main features: X-ray absorption near-edge structure (XANES) and extended X-ray absorption fine structure (EXAFS). XANES offers insights into the electronic and geometric structure and oxidation states of the material, while EXAFS reveals information about the local atomic structure, such as atomic distances and chemical coordination, for specific atomic elements.

This study aims to deliver a morphological and chemical characterization of nanoprecipitates in the ODS ferritic steels combining the capacities of both SANS and XAS.

A SANS experiment was performed using the ZOOM instrument at the Rutherford Appleton Laboratory (experiment RB2310339) [27]. The detector to sample distance was 4 m, the neutron beam size 4 × 4 mm^2, and the beam wavelength varied between 1.75 and 16.5 Å. The experiment was performed at room temperature (RT), applying a saturating magnetic field (H) of ~1.4 T to align the magnetic contributions. Scattering intensities for Batch-I, Batch-II and Batch-III were obtained on squared 1 × 1 cm^2 and 1 mm thickness samples on the transversal-short (TS) and longitudinal-transversal (LT) planes. A two-phase model of a matrix with polydisperse nanoparticles was applied using SasView 5.0.5 [28]. This first part of the model commonly follows a power law. In this region, the scattering function decreases at low momentum transfer (Q), where the contribution of microstructural heterogeneities, ranging around tens of nanometers, and the grain boundaries are included. The second contribution of the model assumes spherical nanoparticles for higher Q values based on a Guinier law approximation [29]. No evidence was found for other nanoparticle geometries. In the presence of a high magnetic field the matrix magnetization is saturated and the magnetic scattering can be experimentally determined from the difference between the scattering intensity contributions perpendicular and parallel to H. The ratio between the magnetic and nuclear sum over the nuclear contribution is defined as the A-ratio, that can provide details about chemical composition, magnetization and atomic density for secondary phases.

XAS data collection was granted at the ALBA synchrotron light source facility located in Cerdanyola del Vallès (Spain) at the BL22-CLAESS beamline. XAS data were collected in fluorescence mode using a 6 channel SDD detector on the ODS materials in final consolidated state, while powder samples were collected in transmission mode. Spectra were acquired at room temperature using a Si311 double crystal monochromator. Spectral processing was carried out with the Athena software package [30]. Energy calibration at Y, Zr, and Fe K-edges and the W-LIII edge was carried out by setting the energy of the first inflection point of the corresponding metallic foil to 7112 eV for Fe, 17038 eV for Y, 17998 eV for Zr and 10207 eV for W. The Fe K-edge was measured up to k = 7.0 $Å^{-1}$, Y K-edge up to k = 15.5 $Å^{-1}$, W LIII-edge up to k = 16.4 $Å^{-1}$ and Zr K-edge up to k = 16.0 $Å^{-1}$.

EXAFS were extracted using the AUTOBK algorithm employing a spline in the 0–16 A^{-1} k-range having a R_{bkg} of 1.3. Hanning based windows were used to obtain the Fourier transforms. The Artemis software was used for EXAFS fitting, employing the FEFF 6.0 code for path generation [29,31]. Theoretical paths were fit using a global S_0^2 value and ΔE_0. Single and multiple scattering paths were fit in terms of Δr and σ^2, which represent the deviation from the expected interatomic distances and the structural disorder, respectively. Multi k-weighting (1,2,3) was used to fit EXAFS spectra. To assess the quality of the fits the R_{factor} and the reduced χ^2 were minimized.

Additional information regarding the SANS and XAS experiments can be found elsewhere [32].

3. Results and discussion

3.1. X-ray diffraction

Fig. 2 and Fig. 3 show the XRD patterns for the Zr-based materials at the different stages of their production route. They are consistent with a single BCC ferritic phase in all cases (14754 file in the FIZ Karlsruhe-

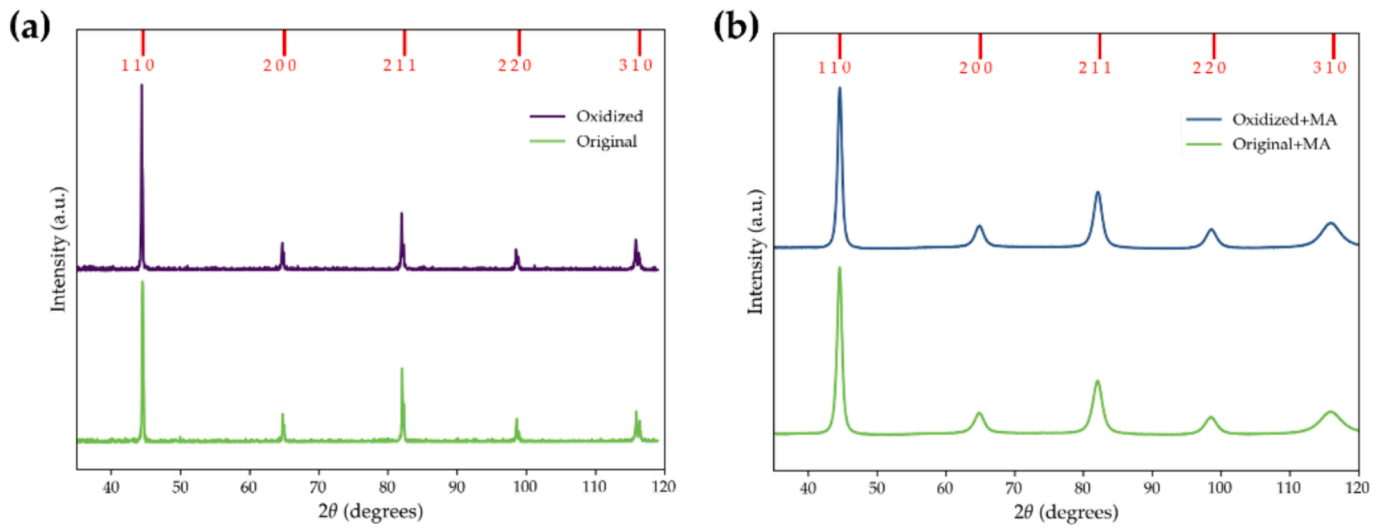

Fig. 2. XRD patterns from the Zr-based original and oxidized atomized powders (a) and mechanically alloyed original and oxidized powders (b). BCC peaks are showed on the top axis in red. (For interpretation of the references to colour in this figure legend, the reader is referred to the web version of this article.)

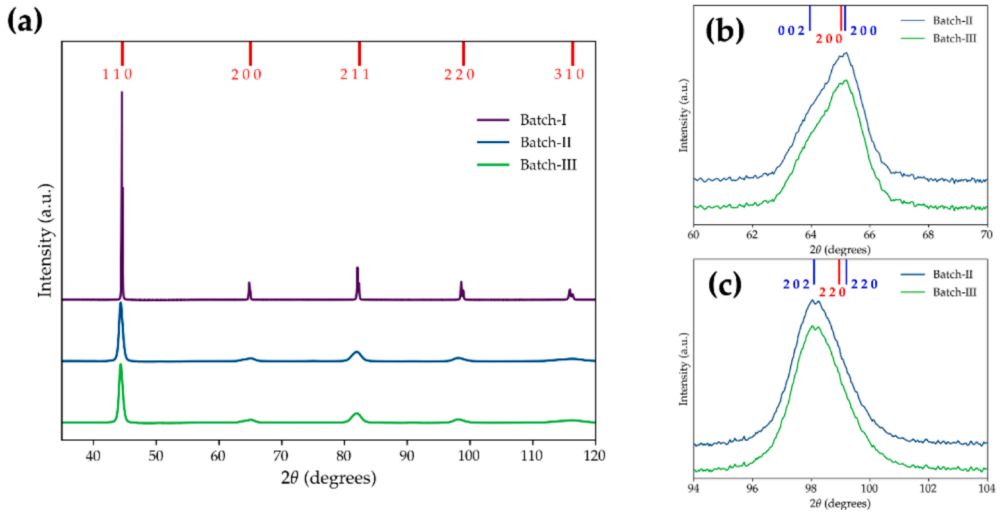

Fig. 3. (a) XRD patterns from the Zr-based consolidated Batch-I, Batch-II and Batch-III ODS steels; (b) and (c) zoom-in XRD patterns from (a). BCC peaks are indicated on the top axis in red and BCT peaks in blue. (For interpretation of the references to colour in this figure legend, the reader is referred to the web version of this article.)

ICSD database [33]). Peaks of the Zr-based original and oxidized powders are very sharp without evident differences among them (Fig. 2 (a)). This behavior remains present for the corresponding consolidated Batch-I (Fig. 3 (a)), being typically associated with a low number of defects and large crystallites (>100 nm). Mechanical alloying broadens the BCC peaks, as seen in the milled powders and the consolidated Batch-II and Batch-III steels (Fig. 2 (b)), associated with small crystallites and induced micro-strains, for example, from dislocations. The full width at half maximum (FWHM) for the original and oxidized powders ranges between 0.2–0.7 (2θ degrees), while for both materials after mechanical alloying the FWHM increases up to 0.7–3.1 (2θ degrees). The FWHM for Batch-I ranges 0.7–1.4 (2θ degrees), for Batch-II 0.9–2.8 (2θ degrees) and for Batch-III 0.9–2.3 (2θ degrees).

Table 2 summarizes the obtained lattice parameters. Their values are very similar and do not vary significantly. The oxidized powder has a slightly larger lattice parameter than the original powder to accommodate the intake of oxygen atoms in the crystal lattice. Mechanical alloying increases the lattice parameter of both original and oxidized powders. After consolidation these differences minimize, matching the same value of the Ti-based ODS sample [23].

Table 2
Calculated lattice parameters for the alpha-ferrite phase for the Zr-based ODS ferritic steel at different stages of its processing route (MA stands for mechanically alloying). Statistical errors lay below 0.1 ‰ [23].

Original powder	Oxidized powder	Oxidized powder + MA	Original powder + MA	Batch I	Batch II	Batch III
2.874 Å	2.877 Å	2.878 Å	2.876 Å	2.873 Å	2.874 Å	2.873 Å

Batch-III presents asymmetric peak shapes regarding the Fe BCC phase (Fig. 3 (b) and Fig. 3 (c)). This could indicate a martensitic body-center-tetragonal (BCT) phase (Powder Diffraction File™ 00-044-1291 [34]). Batch-II peaks seem also slightly asymmetric although to a lower extent. There are no additional clear peaks detected that could be associated with other secondary phases.

3.2. Small angle neutron scattering

The final consolidated Zr-based steels were studied by means of SANS. The scattering intensities associated to the nuclear components for the three batches in the TS and LT planes are displayed in Fig. 4 (a), Fig. 4 (b) and Fig. 4 (c), and Fig. 4 (d), Fig. 4 (e) and Fig. 4 (f), respectively. The nuclear scatterings are obtained at the directions parallel to the applied magnetic field, H (sectors of 30°). Fitting functions to the experimental curves are obtained following a two-phase model (solid lines in Fig. 4 (b), Fig. 4 (c), Fig. 4 (d) and Fig. 4 (f)) as the procedure described in [32], and they are the sum of the dotted and dashed lines for a power law fit and a Guinier-law approximation [35], respectively. Previous studies on the Ti-based ODS steel by TEM and APT, and SANS and XAS reported precipitate sizes for the nanoparticles dispersion that link them with the Guinier-Law approximation in the two-phase model [24,32]. The present study applies the same concept. The nuclear scattering identifies non-magnetic secondary phases as scattering centers. Y-rich oxide nanoprecipitates are non-magnetic precipitates whose contribution is limited to the nuclear scattering component. The scattering curves for Batch-I in both TS and LT planes (Fig. 4 (a) and Fig. 4 (d)) do not show any change in tendency between the power law fit and the Guinier approximation region (see insets in Fig. 4 (a) and Fig. 4 (d)). Thus, they do not exhibit a clear sign of nanoprecipitates presence. Additionally, the fitting process did not converge when using the two-phase model. Therefore, the experimental data was fitted to a single model with only a power law fit in this material (dotted line in Fig. 4 (a) and Fig. 4 (d)), representing the presence of larger secondary phases and the absence of nanoparticles. In Batch-II and Batch-III a signature of oxide nanoparticles is appreciated due to the increase in the scattering intensity at high Q in both TS and LT planes (see figure insets and Fig. 4 (b) and Fig. 4 (c), and Fig. 4 (e) and Fig. 4 (f), respectively). Both materials were fitted with the two-phase model of a power law and a Guinier approximation. The two materials show similar scattering intensities representing similar presence of larger secondary phases and nanoprecipitates.

Table 3 shows the theoretically calculated A-ratios for different secondary phases based on Y-Zr-O chemical compositions in an ODS Fe-14Cr (wt.%) matrix. These results were obtained following the procedure described in [32]. For the present study, the nuclear scattering length used for zirconium is $0.716 \cdot 10^{-12}$ cm. The nuclear plus magnetic scattering component is extracted at the direction perpendicular to H (sectors of 30°). Then, both nuclear and nuclear plus magnetic scattering (Fig. 5) are used to obtain the experimental A-ratios for the three ODS materials.

The obtained A-ratios for Batch-I, Batch-II and Batch-III are shown in Fig. 6. It depicts the A-ratios for all the Q range, although the A-ratios for the nanoparticle dispersion were only obtained from high Q values, as the nanoparticles are linked to the Guinier-Law approximation region, where A-ratios remain at a constant value. The A-ratio for Batch-I could not be obtained in the expected domain of the nanoparticle dispersion. This region is mainly dominated by the signal background in both TS and LT planes, thus, indicating the absence of nanoprecipitates.

The detailed characterization of the nanoparticle dispersion is presented in Table 4. Batch-II is characterized by an A-ratio of 4.0 ± 0.4 on the LT plane and 3.1 ± 0.6 on the TS plane. Batch-III is defined by an A-ratio of 3.9 ± 0.3 on the LT plane and 3.1 ± 0.6 on the TS plane. These results suggest a homogenous A-ratio of 4.0 on the TS plane, and 3.1 on the LT plane. The calculated A-ratio for Y-rich nanoparticles is then linked in both planes with the $Y_2Zr_2O_7$ phase, which exhibits the closest A-ratio to the experimental results. (Table 3). The different crystallographic structures for $Y_2Zr_2O_7$ present A-ratios of 2.71, 4.27 and 4.20. The monoclinic P12_1$\bar{1}$ phase of $Y_2Zr_2O_7$ with an A-ratio of 4.20 was preferentially selected for the calculation of mean radii and volume fractions from fitting functions using SasView software.

Volume fraction and mean radii were obtained with the SasView software by setting the scattering length density and the scattering length density solvent parameters to zero and $2.47 \cdot 10^{-6}$ Å^{-2}, respectively, based on the results present in Table 3 for the monoclinic P12_1$\bar{1}$ $Y_2Zr_2O_7$ phase. The results are summarized in Table 4. Mean radii

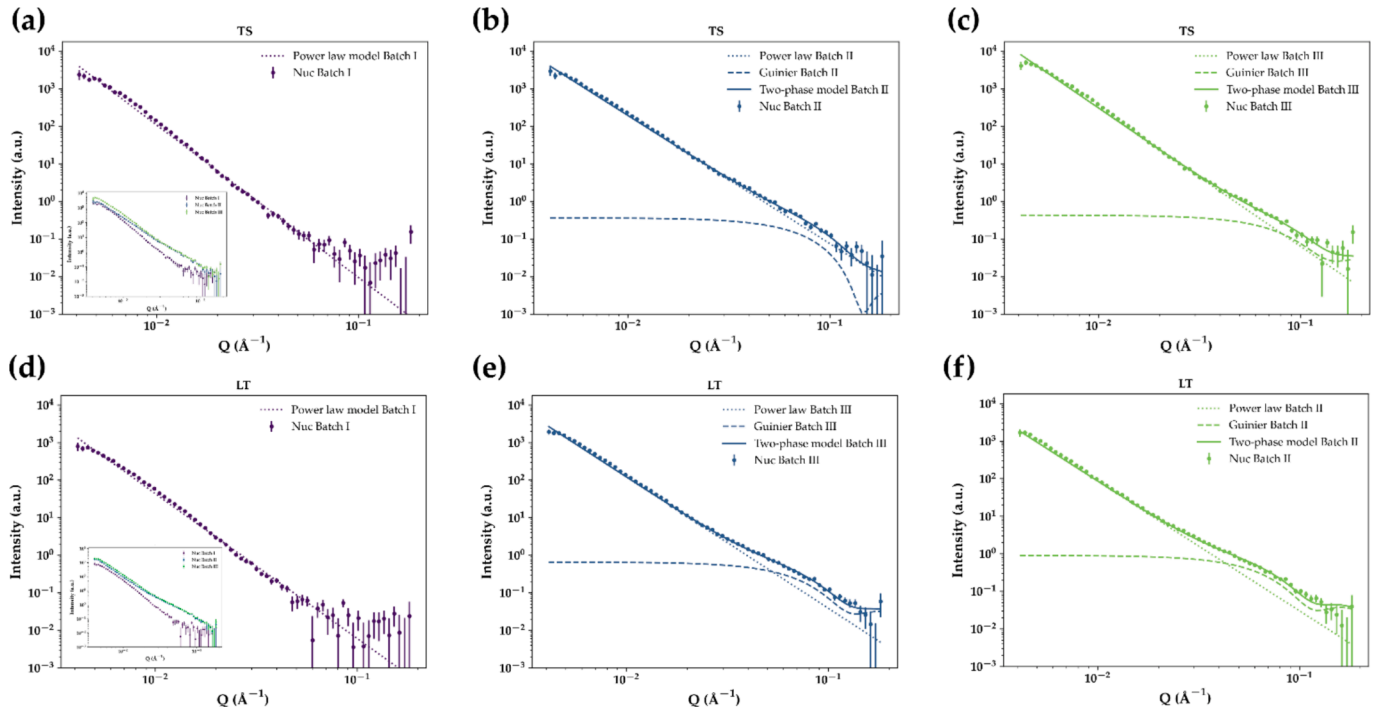

Fig. 4. SANS nuclear scattered intensity for the side-on sample orientation on Batch-I (a) and (d), Batch-II (b) and (e) and Batch-III (c) and (f), on the TS (figures on top) and LT planes (figures at the bottom). Fitting functions are also displayed. The two-phase model (solid line) represents the sum of the power law fit (dotted line) and the Guinier approximation (dashed line).Figure insets in (a) and (d) represent the overlapping experimental results for Batch-I, Batch-II and Batch-III on the TS and LT planes, respectively, for an easier comparison.

Table 3
Theoretically calculated A-Ratio for different Y-rich precipitates in an Fe-14Cr (wt.%) matrix.

Secondary Phase	Structure	V_{at} (cm^3)	$\Delta\rho^2_{nucl}$(cm^{-4})	$\Delta\rho^2_{mag}$(cm^{-4})	A-ratio
$Y_4Zr_3O_{12}$	Triclinic P1	$1.32 \cdot 10^{-23}$	$5.38 \cdot 10^{20}$	$1.96 \cdot 10^{21}$	4.64
$Y_4Zr_3O_{12}$	Triclinic P1	$1.32 \cdot 10^{-23}$	$5.22 \cdot 10^{20}$	$1.96 \cdot 10^{21}$	4.76
$Y_4Zr_3O_{12}$	Triclinic P1	$1.31 \cdot 10^{-23}$	$5.12 \cdot 10^{20}$	$1.96 \cdot 10^{21}$	4.83
$Y_2Zr_2O_7$	Monoclinic C12/m1	$1.69 \cdot 10^{-23}$	$1.14 \cdot 10^{21}$	$1.96 \cdot 10^{21}$	2.71
$Y_2Zr_2O_7$	Cubic Fd$\bar{3}$m1	$1.36 \cdot 10^{-23}$	$6.00 \cdot 10^{20}$	$1.96 \cdot 10^{21}$	4.27
$Y_2Zr_2O_7$	Monoclinic P12_1$\bar{1}$	$1.36 \cdot 10^{-23}$	$6.13 \cdot 10^{20}$	$1.96 \cdot 10^{21}$	4.20
$YZrO_3$	Monoclinic C121	$1.43 \cdot 10^{-23}$	$5.13 \cdot 10^{20}$	$1.96 \cdot 10^{21}$	4.82
$YZrO_3$	Orthorhombic I2_1$\bar{2}$_12$\bar{1}$	$1.44 \cdot 10^{-23}$	$5.31 \cdot 10^{20}$	$1.96 \cdot 10^{21}$	4.69
YZr_4O_9	Triclinic P1	$1.27 \cdot 10^{-23}$	$3.25 \cdot 10^{20}$	$1.96 \cdot 10^{21}$	7.03
YZr_4O_{10}	Tetragonal I4/m	$1.18 \cdot 10^{-23}$	$1.88 \cdot 10^{20}$	$1.96 \cdot 10^{21}$	11.40
YZr_5O_{11}	Monoclinic P1m1	$1.26 \cdot 10^{-23}$	$3.08 \cdot 10^{20}$	$1.96 \cdot 10^{21}$	7.36
YZr_5O_{12}	Monoclinic C121	$1.18 \cdot 10^{-23}$	$1.94 \cdot 10^{20}$	$1.96 \cdot 10^{21}$	11.11
$YZrO_{14}$	Cubic Fd$\bar{3}$m1	$1.31 \cdot 10^{-23}$	$2.99 \cdot 10^{20}$	$1.96 \cdot 10^{21}$	7.55
$Y_2Zr_8O_{19}$	Tetragonal P$\bar{4}$m2	$1.18 \cdot 10^{-23}$	$1.93 \cdot 10^{20}$	$1.96 \cdot 10^{21}$	11.17
YZr_9O_{20}	Triclinic P1	$1.18 \cdot 10^{-23}$	$1.98 \cdot 10^{20}$	$1.96 \cdot 10^{21}$	10.89
$Y_2Zr_9O_{22}$	Monoclinic P1m1	$1.18 \cdot 10^{-23}$	$1.91 \cdot 10^{20}$	$1.96 \cdot 10^{21}$	11.27
$Y_2Zr_{24}O_{51}$	Orthorhombic Pmm2	$1.20 \cdot 10^{-23}$	$2.32 \cdot 10^{20}$	$1.96 \cdot 10^{21}$	9.45
$Y_6Zr_{22}O_{53}$	Orthorhombic Pmm2	$1.24 \cdot 10^{-23}$	$2.80 \cdot 10^{20}$	$1.96 \cdot 10^{21}$	7.99
$Y_6Zr_{22}O_{53}$	Trigonal R3m	$1.24 \cdot 10^{-23}$	$2.74 \cdot 10^{20}$	$1.96 \cdot 10^{21}$	8.14

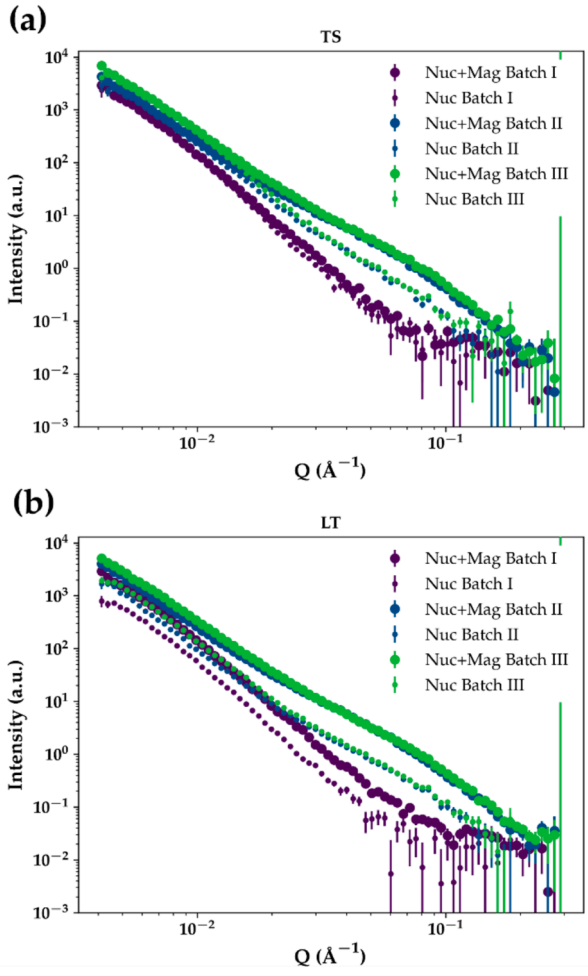

Fig. 5. SANS scattered intensity for the side-on sample orientation on the (a) TS and (b) LT planes.

remain between 3.0 and 3.6 nm for both Batch-II and Batch-III in the different planes. Particularly, the nanoparticle dispersion is slightly more refined in Batch-III. The present analysis shows larger mean radii for the nanoparticles in the Zr-based samples than in the previously characterized Ti-based material, in which the mean nanoparticle radii was 2.45 ± 0.04 nm [32]. Batch-III presents slightly higher volume fractions and number densities of nano oxides than Batch-II, while the Ti-based ODS presented higher values (0.96 ± 0.03 % [32]) than both Batch-II and Batch-III. The substitution of titanium by zirconium in this ODS steel seems to decrease the nanoprecipitates number density while simultaneously increasing their sizes. Additionally, the different results between the TS and LT planes in both Batch-II and Batch-III might be related to the anisotropic properties induced by the HR treatment applied on these materials. HR might modify the nanoparticles morphologies where they are no longer perfect spheroids but ellipsoids, and they exhibit larger axes on the LT plane and shorter axes on the TS one, inducing larger mean radii and sizes in the LT plane than in the TS one.

In Fig. 5, Batch-I presents an increase in the magnetic signal on the LT plane for all Q values (Fig. 5 (b)). This might indicate the presence of magnetic scattering centers preferentially aligned in the rolling direction matching this plane. This magnetic contribution is also present in Batch-II and Batch-III in both TS and LT planes, but restrained at lower Q values.

To assess the effects of HR on the steel microstructure and secondary phases, pairs of data sets were acquired varying the sample orientation 90° perpendicular to the beam axis (horizontal and side-on orientations). The experimental results are depicted in Fig. 7. There is a sign of anisotropies on the TS planes for the three materials (Fig. 7 (a), Fig. 7 (c) and Fig. 7 (e)). Isotropic materials would present overlapping data while comparing the respective experiments from different orientations, i.e., the side-on and horizontal configurations. The observed differences in the scattering intensities, which are more evident in the power law approximation region and linked to the presence of larger precipitates, are a sign of these anisotropies. Additionally, the nuclear scattering curves present higher intensities on the side-on orientation, while the magnetic scattering curves present higher values on the horizontal configuration. Particularly, these anisotropies are more noticeable on

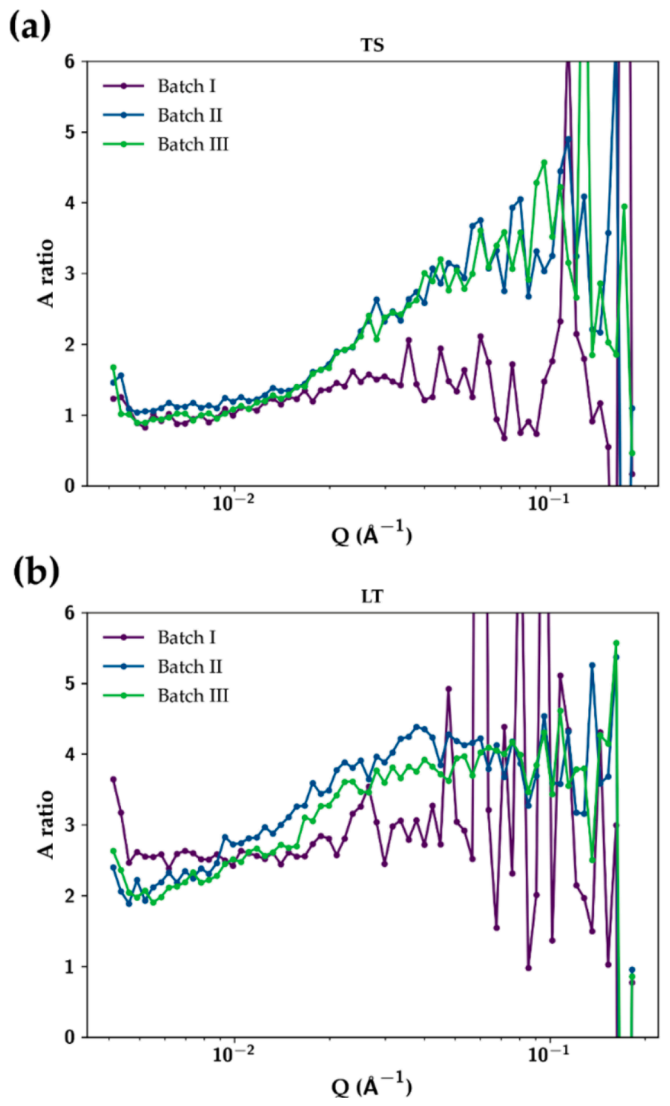

Fig. 6. A-ratio for the side-on sample orientation on the (a) TS and (b) LT planes.

the magnetic scattering signal. This could be associated to the presence of non-magnetic and magnetic scattering centers preferentially aligned in a particular direction. This direction might be induced by grain boundaries as a consequence of the HR (as previously reported in [32]). The regions of Q related to the presence of nanoparticles at the Guinier law region do not show any sign of anisotropies thus, a homogeneous distribution of nano oxides can be expected in Batch-II and Batch-III. It is still worth noting the absence of any sign that could be associated with the presence of oxide nanoparticles in Batch-I at the Guinier approximation region, for any sample orientation or plane. The LT planes do not show nuclear nor magnetic anisotropies, as the scattering intensities comparing the side-on and horizontal configurations overlap; this plane may exhibit a lower microstructural anisotropy after HR (Fig. 7 (b), Fig. 7 (d) and Fig. 7 (f)).

3.3. X-ray absorption spectroscopy

The four powder samples (original, oxidized and original and oxidized with mechanical alloying) and the three final consolidated Zr-based steels (Batch-I, Batch-II and Batch-III) were characterized by means of XAS through the study of the X-ray absorption near edge structure (XANES) and the extended X-ray absorption fine structure (EXAFS).

3.3.1. X-ray absorption near edge structure – XANES

The normalized XANES spectra on the Fe K-edge for the Zr-based material in the different powder samples evidenced a main metallic character of the iron atoms. The four powder samples are very similar and comparable to the metallic iron measured as reference (Supplementary Fig. 1). The metallic bonding of iron atoms remains for Batch-I, Batch-II and Batch-III samples (Supplementary Fig. 2). The absorption edge has an energy of 7112 eV for the three final ODS steel samples, same value as for the reference metallic iron.

Fig. 8, Fig. 9 and Fig. 10 (a) show the results obtained at the Y K-edge. Additionally, three experimental references are included for comparison purposes: metallic yttrium, Y_2O_3, and $Fe_5Y_3O_{12}$. The energy of the absorption edge was selected in the first peak of the first derivate of μ(E). The absorption energies were 17038.0 eV for metallic Y, 17043.5 eV for Y_2O_3 and 17043.0 eV for $Fe_5Y_3O_{12}$.

The analysis of the powder samples is presented in Fig. 8. It is worth noting the high resemblance between the original and oxidized powders, and between these samples after the mechanical alloying process, which causes a similar variation in both samples. The energies at the absorption edge for the powder samples were: 17039.5 eV for the original powder, 17040.1 eV for the oxidized powder, and 17041.6 eV and 17041.4 eV for the original and the oxidized powders after mechanical alloying, respectively.

Average values of oxidation states have been estimated by the Kunzl's law using a linear interpolation of the shift of the edge position with respect to the absorption edge of metallic and oxide references. The original and oxidized powders exhibit a main metallic character, where the oxidation state increases from 0.77^+ to 1.12^+ (Fig. 10 (a)). This represents a 45 % increase that can be associated to the oxidation treatment. The oxidation states keep increasing due to mechanical alloying up to 1.8^+ and 1.91^+ (Fig. 10(a)), respectively, where the differences between samples reduces to 6%. The original and oxidized samples show a XANES rising edge profile reminiscent but not equal to metallic Y. This is supported both by the rising edge energy, which implies an oxidation state between 0.7^+ and 1.1^+, and EXAFS analysis (Table 5) which shows Y-Fe scattering as the principal contribution. This

Table 4
SANS results obtained on Batch-I, Batch-II and Batch-III for the nanoparticle dispersion on the side-on orientation for the TS and LT planes. A-ratio, mean radius, R_m, volume fraction, V_f, and number density, N.

Sample	Orientation	A-ratio	R_m (nm)	V_f (%)	N (m^{-3})
Batch-I	TS	–	–	–	–
	LT	–	–	–	–
Batch-II	TS	3.1 ± 0.6	3.2 ± 0.3	0.45 ± 0.07	(3.3 ± 0.5) · 10^{22}
	LT	4.0 ± 0.4	3.6 ± 0.1	0.71 ± 0.04	(3.6 ± 0.2) · 10^{22}
Batch-III	TS	3.1 ± 0.6	3.0 ± 0.2	0.60 ± 0.01	(5.3 ± 0.1) · 10^{22}
	LT	3.9 ± 0.3	3.3 ± 0.1	0.70 ± 0.04	(4.7 ± 0.2) · 10^{22}

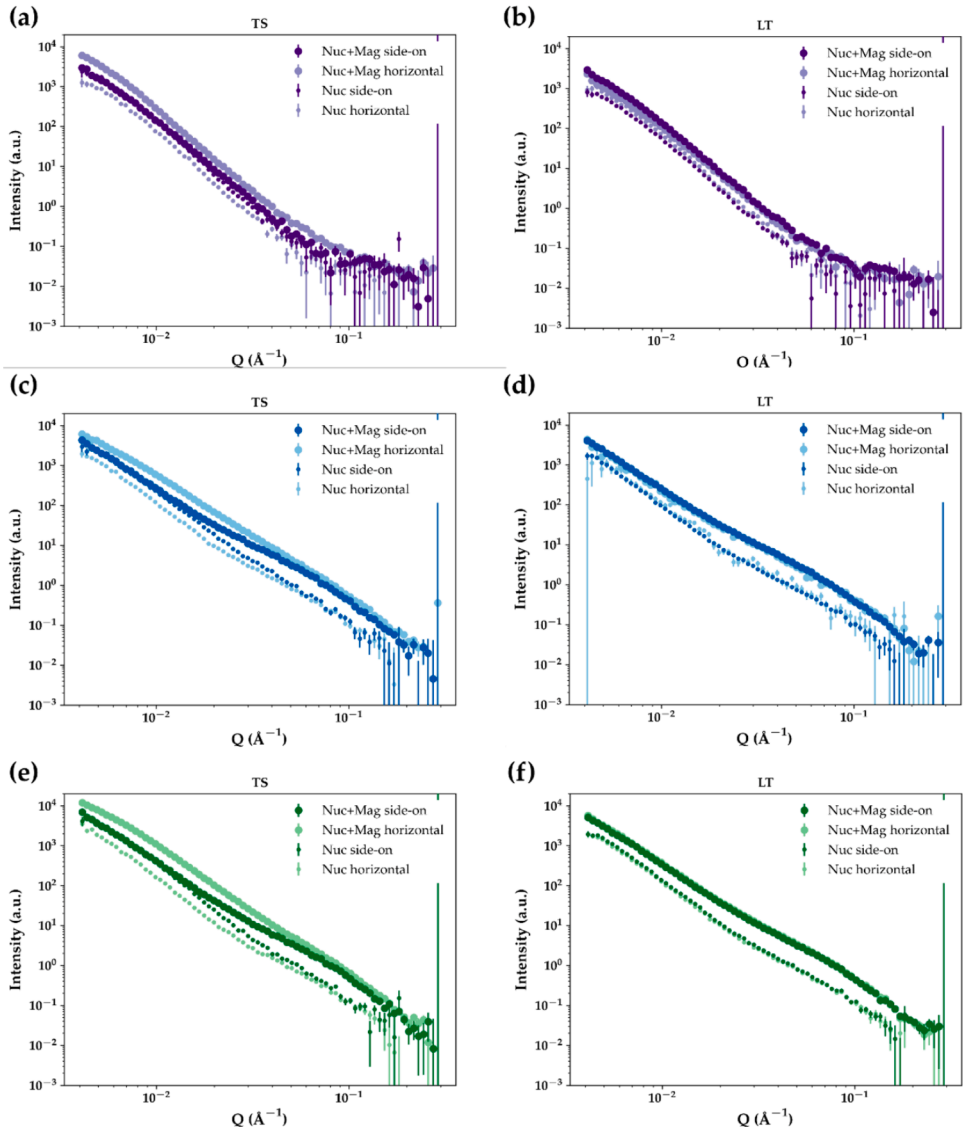

Fig. 7. SANS scattered intensity for the side-on and horizontal sample orientations on Batch-I on the (a) TS and (b) LT planes; Batch-II on the (c) TS and (d) LT planes, and Batch-III on the (e) TS and (f) LT planes.

suggests the presence of low valence Y atoms dispersed in a Fe/Cr matrix. The signal from yttrium atoms evolves to a spectrum very similar to the $Fe_5Y_3O_{12}$ phase after mechanical alloying (or an equivalent phase to this compound) (Fig. 8).

A linear combination fit (LCF) of the different references based on their XANES spectra was performed to elucidate their relative contributions in the different material samples. The LCF showed that the original and oxidized samples have a main metallic character, over 90%, being slightly lower for the oxidized sample, associated to the oxidation treatment. In turn, mechanical alloying caused an evolution in the oxidation state, where the contribution linked to the $Fe_5Y_3O_{12}$ phase (or a similar compatible structure) is now predominant and over 70%.

After consolidation and hot rolling (Fig. 9), the energy values on the absorption edge were 17043.5, 17043.1 and 17043.3 eV for Batch-I, Batch-II and Batch-III, respectively. These values represent an oxidation state of 2.96^+ for Batch-I, 2.83^+ for Batch-II and 2.73^+ for Batch-III, where the Y atoms in the three materials are mainly in form of oxides close to a Y^{3+} value (Fig. 10 (a)). These values are in correspondence with the results reported for the Ti-based ODS in [32]. Batch-I differs from Batch-II and Batch-III samples, which are very similar between them (inset in Fig. 9). Batch-I has a double structure between 17045 and 17060 eV, similar to the Y_2O_3 reference. Batch-II and Batch-III showed a higher maximum absorption peak with lower intense second structures, closer to the $Fe_5Y_3O_{12}$ or a similar structure to this phase. A LCF, using the Y_2O_3 and $Fe_5Y_3O_{12}$ references, suggest a main contribution of the Y_2O_3 phase for Batch-I, around 60 %, while $Fe_5Y_3O_{12}$ (or a compatible compound to this phase) is predominant in Batch-II and Batch-III, around 80 % in both materials. On one hand, the Y signal from Batch-I could be related to the formation of non-nanometric Y_2O_3 precipitates, since the SANS study has not shown presence of any type of nanoprecipitates, while the contribution from other oxides is less important. On the other hand, the precipitation of Y_2O_3 secondary phases is minimum in Batch-II and Batch-III, because the yttrium atoms might form precipitates as, or similar to, the $Fe_5Y_3O_{12}$ reference that might precipitate due to mechanical alloying and is associated with the nanoparticle dispersion.

The influence of zirconium in the oxide nanoparticles formation is key to understand the potential of the processing routes. Zirconium might also be part of the Y-rich nanoprecipitates and would potentially refine their sizes. Fig. 11 and Fig. 12 display the XANES spectra on the Zr K-edge absorption energy obtained for the Zr-based material and different references. The experimental references measured to compare

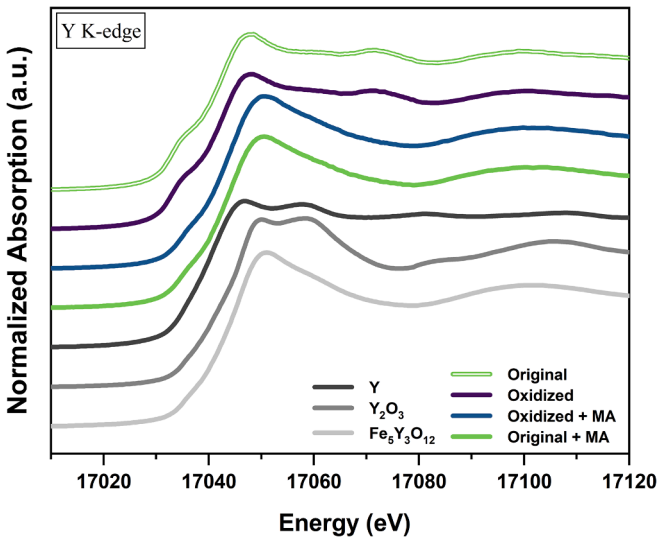

Fig. 8. Normalized XANES spectra on the Y K-edge for the powder samples of the Zr-based material and the experimental references.

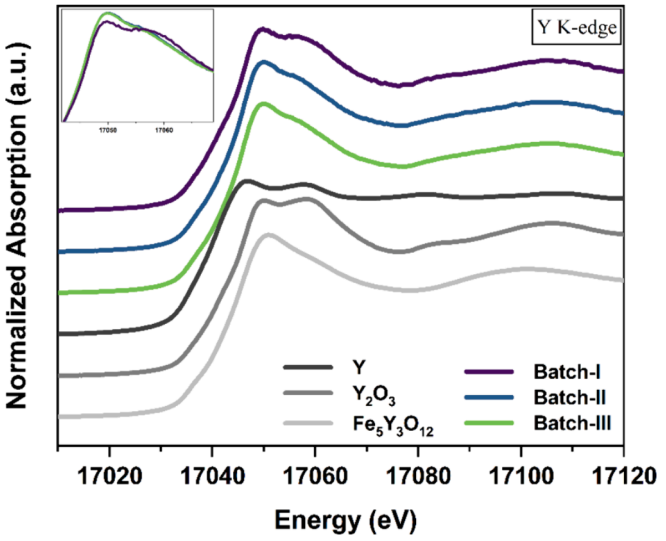

Fig. 9. Normalized XANES spectra on the Y K-edge for the final Zr-based materials and the experimental references. The inset represents the comparison between Batch-I, Batch-II and Batch-III.

the experimental results with different types of secondary phases were metallic zirconium, ZrO_2 and ZrC.

The study of the Zr-based material in powder form on the Zr K-edge presents the same trend observed before for the spectra on the Y K-edge: the original and oxidized powders are very similar and mechanical alloying causes their evolution remaining similar but differing from the previous state. The energy values for the absorption edge were 17988.0 eV for metallic Zr, 18005.2 eV for ZrO_2 and 18001.5 eV for ZrC. The energy for the absorption edge obtained was 17999.2 eV for the original powder, 17999.5 eV for the oxidized powder, 18001.9 eV for the original powder after mechanical alloying and 18002.2 eV for the oxidized powder after mechanical alloying. The signal from zirconium atoms at the original and oxidized powders is mainly metallic with mean oxidation states increasing from 0.75^+ to 0.91^+, respectively, after the oxidation treatment (Fig. 10 (b)). After mechanical alloying, mean oxidation states keep increasing up to 2.25^+ and 2.41^+ for the original and oxidized powders, respectively (Fig. 10 (b)). The experimental spectra for the alloyed powders are now more similar to the ZrO_2 reference although the contribution from metallic Zr atoms is still noticeable on the XANES spectra and the oxidation state values.

The LCF on these samples on the Zr K-edge showed that the original and oxidized samples are characterized by a predominant metallic character, over 80%. After oxidation, the oxidized powder slightly lowers its metallic character. Mechanical alloying produces a significant oxidation in both samples where the original and oxidized powders after alloying present a metallic character around 40%. This change matches with an increase of the component associated to the oxides up to around 50%. ZrC was considered but does not contribute to the fit outcome.

Fig. 12 shows experimental spectra of the final consolidated Zr-based steels. XANES spectra on the Zr K-edge maintain the same trend as in the Zr K-edge, where Batch-II and Batch-III are very similar between them but differ from Batch-I. The mean oxidation state for Batch-I is 2.52^+, lower than the oxidation states for Batch-II and Batch-III, 3.75^+ and 3.86^+, respectively (Fig. 10 (b)). The mean oxidation state of zirconium atoms in Batch-I indicates that the contribution of zirconium atoms forming metallic bonds is considerably high, meaning that a considerable amount of zirconium forms metallic secondary phases, minimizing the proportion of zirconium used for the formation and refinement of oxide nanoparticles. In contrast, the mean oxidation state in Batch-II and Batch-III is very close to the expected oxidation state of a contribution obtained from Y-rich nanoparticles (Fig. 10 (b)) suggesting their formation in a higher amount in these materials.

The spectra obtained on the W LIII-edge for the Zr-based materials and the experimental references are shown in Supplementary Fig. 3 and Supplementary Fig. 4. The powder samples in Supplementary Fig. 3 highlight the main metallic character of tungsten atoms in the four materials because of the high resemblance with the metallic tungsten reference. The results on the absorption edge for all the powder samples

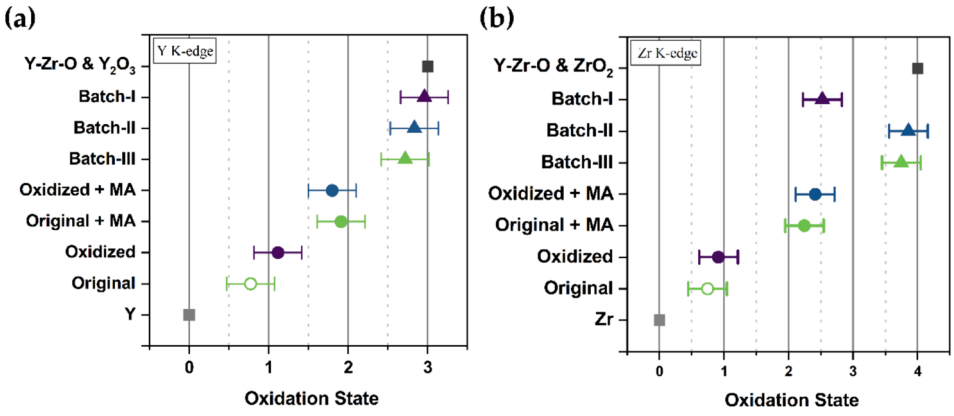

Fig. 10. Mean oxidation states of (a) Y and (b) Zr atoms as a function of the processing route, together with different references.

Table 5
EXAFS results on the powder samples of the Zr-based material and experimental references at the Y K-edge (MA stands for mechanically alloying). Theoretical values of Y-based references obtained from CIF files are included for comparison [36] (MP stands for the Materials Project database reference).

Sample	Element	N	R_{eff} (Å)	σ^2 (Å^2)	R-factor
Original experimental	Fe	7.7(1.1)	2.79(1)	0.020(2)	0.0101
Oxidized experimental	Fe	5.6(2.2)	2.76(2)	0.016(3)	0.0076
Original + MA experimental	O1	2.3(1)	2.25(1)	0.003(1)	0.0091
	O2	1.2(1)	2.41(1)	0.002(2)	
	Total O	3.6(1)	2.30(1)	0.003(1)	
	Fe	1.0(1.0)	2.60(6)	0.001(6)	
	Fe + Y	9.6(2.3)	3.23(2)	0.011(2)	
Oxidized + MA experimental	O1	2.4(1)	2.25(1)	0.003(1)	0.0074
	O2	0.9(1)	2.41(1)	0.001(1)	
	Total O	3.3(1)	2.29(1)	0.002(1)	
	Fe	2.1(1.2)	2.64(4)	0.003(3)	
	Fe + Y	4.7(1.1)	3.21(2)	0.005(2)	
Y theoretical (MP: 112)	Y	12	3.602		
Y_2O_3 theoretical (MP: 2652)	O	6	2.304		
	Y	6	3.557		
$Fe_5Y_3O_{12}$ theoretical (MP: 4704)	O	8	2.426		
	Fe + Y	14	3.595		

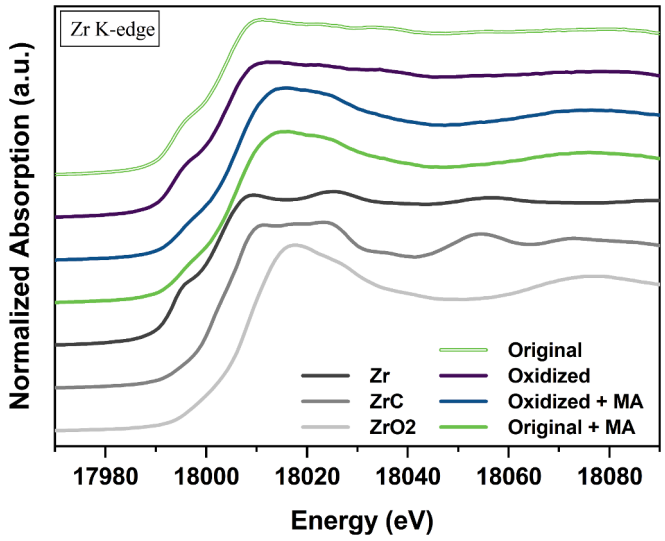

Fig. 11. Normalized XANES spectra on the Zr K-edge for the powder samples of the Zr-based material and the experimental references.

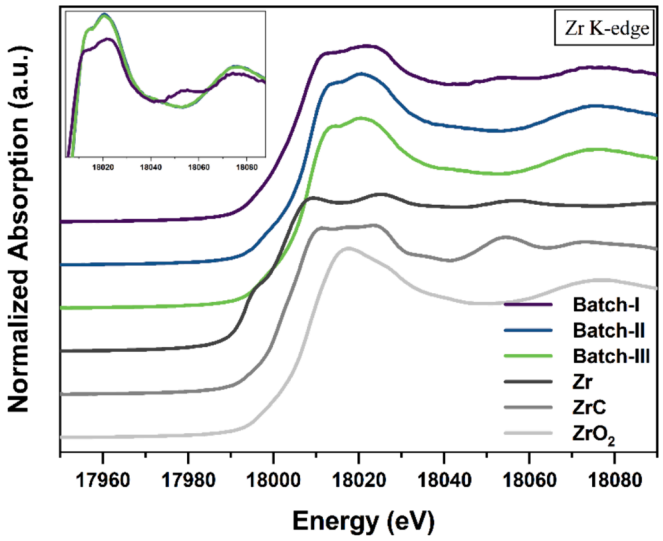

Fig. 12. Normalized XANES spectra on the Zr K-edge for the final Zr-based materials and the experimental references. The inset represents the comparison between Batch-I, Batch-II and Batch-III.

lay around 10207 eV, which is the same value used for calibration in the metallic tungsten reference. Neither mechanical alloying or consolidation and rolling (Supplementary Fig. 4) cause a significant impact on the evolution of tungsten rich precipitates, that remain predominantly forming metallic bonds.

3.3.2. *Extended x-ray absorption fine structure – EXAFS*

The Fourier transform EXAFS data for the Y K-edge as a function of the distance are depicted in Fig. 13 and Fig. 14 for the powder and consolidated samples, respectively. Fitting functions obtained with the Artemis software are also included (Fig. 14). The fitting model for the original and oxidized powders used in Fig. 13 (a) is based in a Y-Fe path centered at 2.75 Å. Small contributions for Y-O and Y-Y paths appear at 2.10 Å and 3.50 Å, respectively, although they have not been considered in the fit due to their small intensities. The fitting model for the mechanically alloyed powders is based on a first shell with two contributions of oxygen neighbors and a second shell with a combination of iron and yttrium atoms. First contribution of oxygen atoms has N = 4, centered at 2.278 Å; the second contribution has N = 2, centered at 2.357 Å. At the second shell the contribution of iron atoms is centered at 2.750 Å and the contribution of yttrium at 3.557 Å. The $Fe_5Y_3O_{12}$ spectrum is used as reference to obtain the experimental results of the amplitude $S_0^2 = 0.805$, and the energy values, $\Delta E_0 = -7.06$ eV. Experimental data were fitted in the R range between 1.4 and 3.8 Å. The experimental results are summarized in Table 5 and Table 6.

The same trend previously observed in the XANES section is still present in both Fig. 13 and Fig. 14. The original and oxidized powders

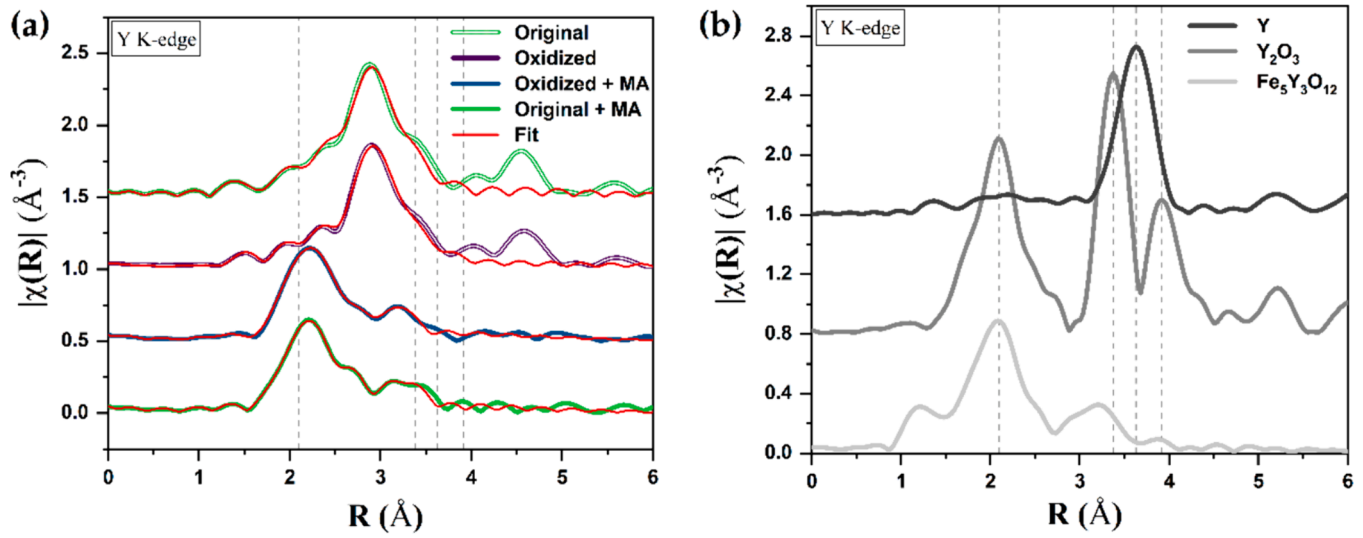

Fig. 13. Fourier transform magnitude of k^2-weighted EXAFS oscillations on the Y K-edge for the powder samples of the Zr-based material (a) and a comparison with the experimental references (b). Vertical dash lines are included on references peaks for an easier comparison. First Y-O scattering path from Y_2O_3 has been used for phases correction.

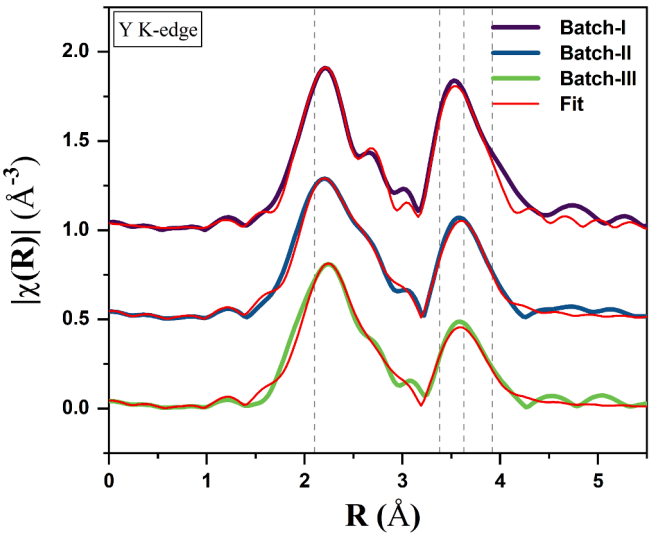

Fig. 14. Fourier transform magnitude of k^2-weighted EXAFS oscillations on the Y K-edge for the final Zr-based materials. Vertical dash lines are included on reference peaks for an easier comparison. First Y-O scattering path from Y_2O_3 has been used for phases correction.

are very similar; after mechanical alloying both samples evolve similarly; and after consolidation and rolling Batch-I differs from Batch-II and Batch-III. The original and oxidized powders present a main metallic contribution for iron atoms centered around 2.78 Å and a very low signal from oxygen atoms. The low amount of first oxygen neighbors observed in these powders might restrain the formation of oxide precipitates and thus, be responsible of the lower number of nanoparticles present in Batch-I compared to Batch-II and Batch-III, as previously confirmed in the SANS experiment. Mechanical alloying promotes oxidation in both samples, as illustrated by the peak centered at 2.10 Å, while the signal of metallic iron lowers considerably.

EXAFS results for the final consolidated materials are displayed in Fig. 14. Batch-I has a slightly lower value for first oxygen neighbors, in comparison with Batch-II and Batch-III, and the mean distances are very similar for the three samples. The Debye-Waller factor is higher for Batch-II and Batch-III, which might indicate a higher dispersion in distances for yttrium neighbor atoms. Moreover, the Debye-Waller factor increases in one order of magnitude for the second shell, then the structure is highly distorted at the second order. Mean distances for the second shell are very similar for the three materials and, particularly, Batch-I presents a considerably higher amount of Y + Zr neighbors than Batch-II and Batch-III. This might indicate the presence of different secondary phases in this material compared to Batch-II and Batch-III, that remain very similar.

Table 6
Experimental EXAFS results on Batch-I, Batch-II and Batch-III at the Y K-edge.

Sample	Element	N	R_{eff} (Å)	σ^2 (Å^2)	R-factor
Batch-I experimental	O1	4.9(4)	2.25(1)	0.002(1)	0.0318
	O2	2.5(4)	2.42(1)	0.001(2)	
	Total O	7.4(4)	2.30(1)	0.002(1)	
	Y + Zr	15.0(1.4)	3.58(1)	0.013(1)	
Batch-II experimental	O1	5.2(2)	2.25(1)	0.004(1)	0.0089
	O2	3.4(2)	2.41(1)	0.003(1)	
	Total O	8.6(2)	2.30(1)	0.004(1)	
	Y + Zr	10.7(7)	3.61(1)	0.014(1)	
Batch-III experimental	O1	4.6(2)	2.25(1)	0.004(1)	0.0137
	O2	3.2(3)	2.39(1)	0.004(1)	
	Total O	7.9(3)	2.30(1)	0.004(1)	
	Y + Zr	10.4(1.0)	3.60(1)	0.015(1)	

The results on the Zr absorption K-edge for the EXAFS region are displayed in Fig. 15 and Fig. 16. The fitting model for the original and oxidized powders is based on the Zr_6Fe_{23} (M.P.: 582926) structure with N = 8 and N = 4 iron atoms at the first shell, centered at 2.885 Å and 2.983 Å, respectively. The second shell was defined by a Zr-Zr path with N = 4, centered at 3.396 Å and a Zr-Fe path, with N = 1, centered at 3.469 Å. The fitting model for the mechanically alloyed powders obtained with the Artemis software is based on the ZrO_2 experimental reference. It is configured by a first shell with three oxygen signals with N = 2, N = 3 and N = 2, centered at 2.062 Å, 2.166 Å and 2.261 Å, respectively. The second shell has two components, the first with iron atoms with N = 1, centered at 2.750 Å and the second of zirconium atoms with N = 12 centered at 3.224 Å. The experimental results are summarized in Table 7 and Table 8.

The original and oxidized powders are almost identical, as well as both samples after mechanical alloying (Fig. 15). The original and

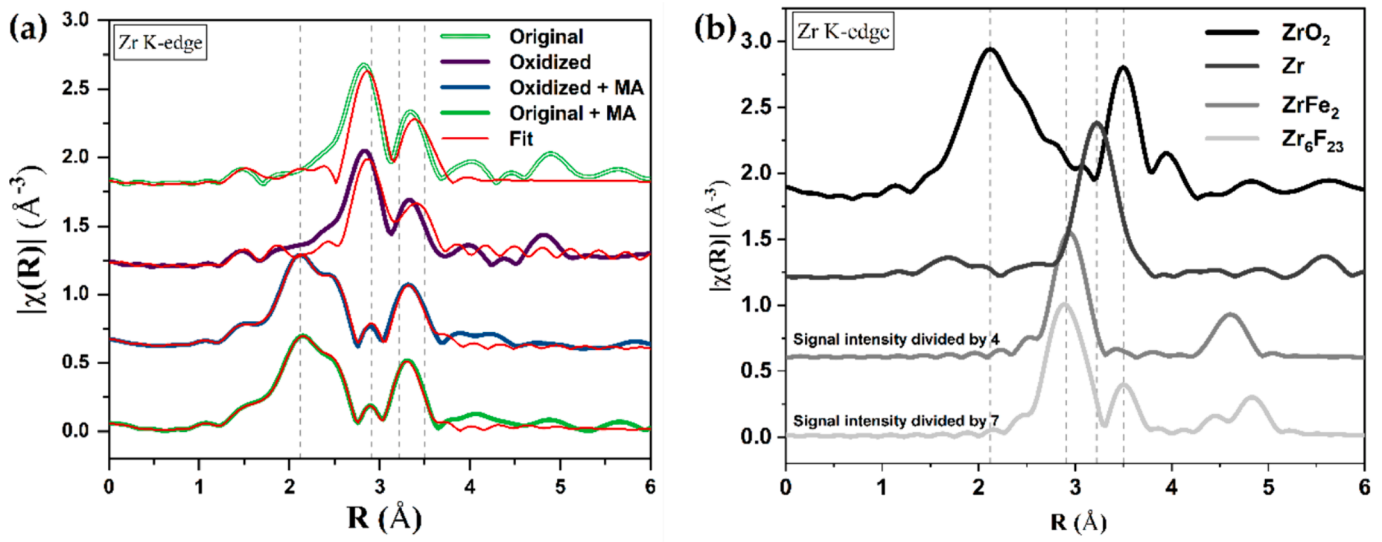

Fig. 15. F Fourier transform magnitude of k^2-weighted EXAFS oscillations on the Zr K-edge for the powder samples of the Zr-based material (a) and a comparison with the experimental references (b). The signals intensity for the $ZrFe_2$ and Zr_6Fe_{23} are divided by 4 and 7 for comparison purposes, respectively. Vertical dash lines are included on references peaks for an easier comparison. First Zr-O scattering path from ZrO_2 has been used for phases correction.

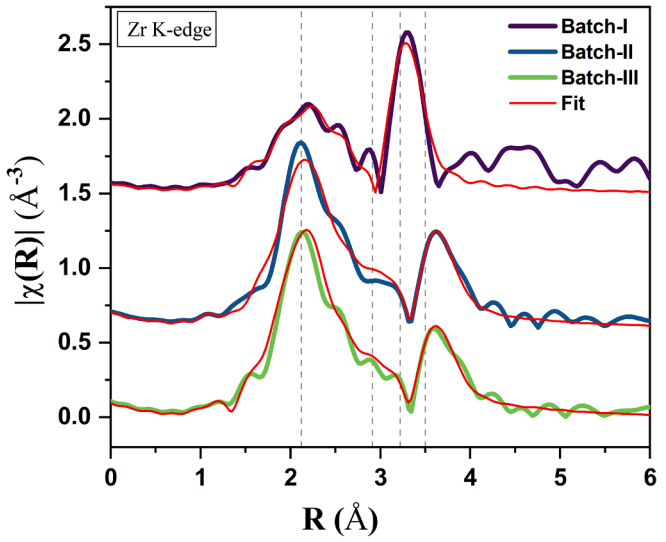

Fig. 16. F Fourier transform magnitude of k^2-weighted EXAFS oscillations on the Zr K-edge for the final Zr-based materials. Vertical dash lines are included on reference peaks for an easier comparison. First Zr-O scattering path from ZrO_2 has been used for phases correction.

oxidized powders have a main metallic character (previously seen in Fig. 10 (b)). Fig. 15 depicts the Fourier transform of the theoretical EXAFS signal simulated for different compounds. The signals of the original and oxidized powders are very similar to the Zr_6Fe_{23} phase although with a considerably lower intensity (the Zr_6Fe_{23} signal is seven times higher than the represented in Fig. 15). Thus, the number of neighbors obtained from the fitting analysis is much smaller for the powders samples than in the reference compound. This could be explained by a nanostructuration of the powder materials or by the presence of a different phase stoichiometries or other compounds (as for example $ZrFe_2$ M.P.: 1718). The oxidation treatment did not cause a significant impact on mean interatomic distances; however, mechanical alloying did.

The original and oxidized powders show two main peaks centered at 2.75 and 3.27 Å associated with the metallic bounds of iron and chromium, and zirconium and yttrium, respectively. The separation between these two peaks is related to the different atomic sizes of these chemical elements. Additionally, there is no clear evidence of any peak around 2 Å from oxygen atoms. After mechanical alloying, this peak associated to oxygen atoms arises in both samples forming the structure observed between 2.0 and 2.5 Å. A second peak is present around 3.3 Å, similar to one of the peaks of metallic bonds observed on the powder before alloying.

The zirconium signal in the original and oxidized powders could be interpreted with a main metallic character formed by the combination of lighter metallic elements as iron and chromium, and heavier ones like yttrium, tungsten and zirconium itself. Mechanical alloying induces the main oxidation of the samples and the second neighbors associated with the metallic peaks evolve to form a unique peak. Now, this peak might only be related with the heavier metallic elements previously mentioned.

The Fourier transform magnitude EXAFS spectra for the steels in final consolidated states are displayed in Fig. 16. The fitting functions are modeled with the Artemis software using a simple model based on the ZrO_2 reference. The model uses a first shell with a unique oxygen signal with N = 7, centered at 2.165 Å, that includes three different signals of oxygen neighbors; and a second shell also with a unique contribution of zirconium atoms with N = 7, centered at 3.452 Å, that includes four different signals of zirconium neighbors. In the case of Batch-II and Batch-III samples there is an additional component at the second shell of oxygen atoms with N = 3, centered at 3.754 Å. The experimental result for the ZrO_2 samples is adjusted and used as reference to obtain the experimental results of $S_0^2 = 0.954$, and the energy values, $\Delta E_0 = -2.24$ eV. Experimental data were fitted in the R range between 1.4 and 3.7 Å.

The EXAFS results for Batch-II and Batch-III are again very similar between them but differing from Batch-I. For the three materials, first oxygen neighbors are centered around 2.2 Å. However, the signal intensity is much lower for Batch-I, than for Batch-II and Batch-III, and the Debye-Waller factor is contrarily higher in Batch-I. This lower intensity but higher Debye-Waller factor might suggest the same number of first oxygen neighbors in Batch-I compared to Batch-II and Batch-III; and additionally, the higher Debye-Waller factor would explain a big dispersion of oxygen atoms in Batch-I.

The second shell is also very different for Batch-I. The second shell for Batch-I is centered at around 3.3 Å, while Batch-II and Batch-III present this shell at higher distances (around 3.5 Å), meaning that it might be formed by two different contributions. The second shell is very

Table 7
Experimental EXAFS on the powder samples of the Zr-based material at the Zr K-edge (MA stands for mechanically alloying). Theoretical values of Zr-based references obtained from CIF files are included for comparison [36] (MP stands for the Materials Project database reference).

Sample	Element	N	R_{eff} (Å)	σ^2 (Å^2)	
Original experimental	Fe + Cr	3.5(8)	2.94(1)	0.002(2)	0.0209
	Zr + Y	2.1(9)	3.36(2)	0.003(2)	
Oxidized experimental	Fe + Cr	3.2(8)	2.94(1)	0.001(2)	0.0726
	Zr + Y	1.6(8)	3.36(3)	0.001(2)	
Original + MA experimental	O1	0.9(4)	2.05(3)	0.007(1)	0.0156
	O2	1.5(3)	2.15(1)		
	O3	1.1(5)	2.25(2)		
	Total O	3.5(1.2)	2.16(2)		
	Fe + Cr	2.3(6)	2.79(2)	0.002(1)	
	Y + Zr	3.4(1)	3.18(1)	0.007(1)	
Oxidized + MA experimental	O1	1.2(7)	2.06(4)	0.003(1)	0.0182
	O2	1.5(3)	2.15(1)		
	O3	1.3(7)	2.26(2)		
	Total O	4,0(1.7)	2.16(3)		
	Fe + Cr	2.4(7)	2.78(1)	0.002(1)	
	Y + Zr	3.5(6)	3.19(1)	0.008(1)	
Zr theoretical (MP: 131)	Zr	6	3.191		
	Zr	6	3.239		
ZrO_2 theoretical (MP: 10735)	O1	2	2.062		
	O2	3	2.166		
	O3	2	2.261		
	Total O	7	2.163		
	Zr	7	3.458		
$ZrFe_2$ theoretical (MP: 1718)	Fe	12	2.941		
	Zr	4	3.072		
Zr_6Fe_{23} theoretical (MP: 582926)	Fe	12	2.918		
	Zr	4	3.396		

Table 8
Experimental EXAFS results on the Zr K-edge.

Sample	Element	N	R_{eff} (Å)	σ^2 (Å^2)	R-factor
Batch-I experimental	O	6.1(1.0)	2.17(2)	0.020(3)	0.0120
	Zr + Y	6.5(9)	3.29(1)	0.008(1)	
Batch-II experimental	O1	6.2(3)	2.15(1)	0.012(1)	0.0271
	Zr + Y	8.5(2.6)	3.53(1)	0.012(2)	
	O2	3.5(3.6)	3.52(4)	0.014(16)	
Batch-III experimental	O1	6.4(3)	2.15(1)	0.012(1)	0.0234
	Zr + Y	8.2(1.2)	3.53(1)	0.013(1)	
	O2	2.9(1.3)	3.55(4)	0.012(9)	

well defined and more intense in Batch-I, but the number of first zirconium neighbors is 31 % and 26 % higher in Batch-II and Batch-III. The higher Debye-Waller factor implies a higher dispersion of zirconium atoms in Batch-II and Batch-III together with a lower intensity, although obtaining a higher number of zirconium neighbors than in Batch-I.

Supplementary Fig. 5 depicts a summary of different phases reported in the literature as crystallographic structures for Y-rich nanoparticles in ODS steels [20]. These are theoretically obtained from their respective CIF files [36]. The signal from oxygen neighbors centered around 2.15 Å matches the signal experimentally obtained in the mechanically alloyed powders and the consolidated materials. Additionally, the main signal from Zr + Y atoms over 3.5 Å could be associated to the signal from these atoms in Batch-II and Batch-III. Contrarily, Batch-I do not show a similar peak supporting the absence or limited number of Y-rich nanoparticles in this alloy, and regarding the mechanically alloyed powders this signal lays at lower distances. $Y_2Zr_2O_7$, $YZrO_3$ and YZr_4O_9 show similar trends to Batch-II and Batch-III alloys, where EXAFS cannot prioritize any of those three as main nanoparticle candidate. The nanometric sizes of these oxides in these two steels could infer disparities when comparing the experimental results with the theoretical EXAFS representations.

4. Conclusions

The production and initial characterization of a new ODS RAF steel based on the alloying of zirconium has been addressed to assess potential benefits of the newly developed STARS route on the microstructure of this structural material candidate. The most important results are:

- The nominal composition Fe-14Cr-2W-0.3Zr-0.24Y (wt.%) was selected to explore the possible benefits of zirconium as substituent of the typically used titanium, as key elements in the precipitation and refinement of the nanoparticles dispersion.
- Three different processing routes were used to compare the production of ODS steel avoiding mechanical alloying, as the STARS route, with the traditional process of blending prealloyed and nanosized powders through mechanical alloying. Under the experimental conditions outlined in this study, dispersion of nanoparticles was only observed in the materials undergoing mechanical alloying.
- SANS analysis pointed out the absence of oxide nanoparticles in Batch-I. Whereas Batch-II and Batch-III do contain nanoprecipitates with slightly larger sizes and lower number densities than in a

previously characterized ODS steel based in titanium alloying. The calculated A-ratio for Y-rich nanoparticles agrees with the phase $Y_2Zr_2O_7$.

- Mechanical alloying increases the oxidation state of Y and Zr atoms minimizing their initial differences induced by the previous oxidation process. After HIP and HR, the oxidation states in Batch-II and Batch-III are very similar and differ from Batch-I.
- EXAFS characterization of the original and oxidized powder materials studied on the Y K-edge present metallic Y atoms dispersed in a Fe/Cr matrix. The low amount of first oxygen neighbors observed in the oxidized powder might restrain the formation of nanometric oxide precipitates in Batch-I, as reported by SANS. After mechanical alloying Y atoms exhibit a signal equivalent to a complex phase similar to $Fe_5Y_3O_{12}$.
- Batch-I showed a main contribution of a Y_2O_3 phase, non-nanometric based on the SANS results, while the $Fe_5Y_3O_{12}$ structure, or a similar complex structure, related with the oxide nanoparticles remains predominant in Batch-II and Batch-III
- The signal from zirconium atoms at the original and oxidized powders is mainly metallic, formed by the combination of lighter metallic elements as iron and chromium, and heavier ones like yttrium, tungsten and zirconium itself. The alloyed powders are more similar to the ZrO_2 reference although the contribution from metallic Zr atoms is still noticeable.
- A considerable amount of zirconium atoms in Batch-I may form metallic secondary phases, minimizing the proportion of zirconium for the formation and refinement of oxide nanoparticles. In contrast, Zr mean oxidation states in Batch-II and Batch-III are very close to the expected oxidation state of Y-rich nanoparticles pointing to their presence in these samples.
- XAS further confirmed the absence of Zr-rich oxide nanoprecipitates in Batch-I, while suggesting the presence of Zr-rich nanometric precipitates in Batch-II and Batch-III.

CRediT authorship contribution statement

M. Oñoro: Writing – review & editing, Writing – original draft, Visualization, Investigation, Formal analysis, Data curation, Conceptualization. **E. Salas-Colera:** Writing – review & editing, Writing – original draft, Visualization, Supervision, Methodology, Investigation, Funding acquisition, Formal analysis, Data curation, Conceptualization. **S.R. Parnell:** Writing – review & editing, Visualization, Supervision, Methodology, Investigation, Funding acquisition, Formal analysis, Data curation, Conceptualization. **V. Martin-Diaconesu:** Writing – review & editing, Visualization, Formal analysis, Data curation, Conceptualization. **D. Alba Venero:** Writing – review & editing, Visualization, Methodology, Formal analysis, Data curation, Conceptualization. **T. Leguey:** Writing – review & editing, Investigation, Funding acquisition, Formal analysis, Conceptualization. **V. de Castro:** Writing – review & editing, Investigation, Funding acquisition, Formal analysis, Conceptualization. **M.A. Auger:** Writing – review & editing, Visualization, Validation, Supervision, Investigation, Funding acquisition, Formal analysis, Conceptualization.

Declaration of competing interest

The authors declare that they have no known competing financial interests or personal relationships that could have appeared to influence the work reported in this paper.

Data availability

Data will be made available on request.

Acknowledgements

Funding from AEI (Agencia Estatal de Investigación) with reference AEI/10.13039/501100011033 (project PID2019-105325RB-C33); Comunidad de Madrid (Spain) through the programs Talento-CAM (2017-T1/IND-5439 and 2021-5A/IND-20954), Technofusion (III) CM (S2018/EMT-4437) and multiannual agreements with UC3M ("Excelencia para el Profesorado Universitario"-EPUC3M14 and "Fostering Young Doctors Research" NANOSOLREC programs); and the V PRICIT (Research and Technological Innovation Regional Program) is gratefully acknowledged. Funding for APC was partially granted by Universidad Carlos III de Madrid (Agreement CRUE-Madroño 2024). Prof. Dr. Ir. J. Sietsma is acknowledged for providing constructive comments to this work. This work benefited from the use of the SasView application, originally developed under NSF award DMR-0520547. SasView also contains code developed with funding from the European Union's Horizon 2020 research and innovation programme under the SINE2020 project, grant agreement No 654000. Authors thanks ALBA-CLAESS staff for providing support during experiment ID: 2021095333.

Appendix A. Supplementary material

Supplementary data to this article can be found online at https://doi.org/10.1016/j.nme.2024.101713.

References

[1] S. Liu, C.U. Segre, G.R. Odette, Characterization of oxide dispersion-strengthened steels by x-ray absorption spectroscopy, Transaction of the American Nuclear Society, 2008, p. 1067, https://www.researchgate.net/publication/224975629.
[2] S.J. Zinkle, G.S. Was, Materials challenges in nuclear energy, Acta Mater. 61 (2013) 735–758, https://doi.org/10.1016/J.ACTAMAT.2012.11.004.
[3] Z. Oksiuta, P. Hosemann, S.C. Vogel, N. Baluc, Microstructure examination of Fe-14Cr ODS ferritic steels produced through different processing routes, J. Nucl. Mater. 451 (2014) 320–327, https://doi.org/10.1016/j.jnucmat.2014.04.004.
[4] S.J. Zinkle, J.T. Busby, Structural materials for fission & fusion energy, Mater. Today 12 (2009) 12–19, https://doi.org/10.1016/S1369-7021(09)70294-9.
[5] Z. Oksiuta, P. Olier, Y. de Carlan, N. Baluc, Development and characterisation of a new ODS ferritic steel for fusion reactor application, J. Nucl. Mater. 393 (2009) 114–119, https://doi.org/10.1016/J.JNUCMAT.2009.05.013.
[6] G.R. Odette, Recent progress in developing and qualifying nanostructured ferritic alloys for advanced fission and fusion applications, J. Miner. Met. Mater. Soc. 66 (2014) 2427–2441, https://doi.org/10.1007/s11837-014-1207-5.
[7] R. Lässer, N. Baluc, J.L. Boutard, E. Diegele, S. Dudarev, M. Gasparotto, A. Möslang, R. Pippan, B. Riccardi, B. van der Schaaf, Structural materials for DEMO: the EU development, strategy, testing and modelling, Fusion Eng. Des. 82 (2007) 511–520, https://doi.org/10.1016/j.fusengdes.2007.06.031.
[8] D. Maisonnier, I. Cook, S. Pierre, B. Lorenzo, D.P. Luigi, G. Luciano, N. Prachai, P. Aldo, DEMO and fusion power plant conceptual studies in Europe, Fusion Eng. Des. 81 (2006) 1123–1130, https://doi.org/10.1016/j.fusengdes.2005.08.055.
[9] S. Ukai, M. Fujiwara, Perspective of ODS alloys application in nuclear environments, J. Nucl. Mater. 307–311 (Part 1) (2002) 749–757, https://doi.org/10.1016/S0022-3115(02)01043-7.
[10] N. Baluc, J.L. Boutard, S.L. Dudarev, M. Rieth, J.B. Correia, B. Fournier, J. Henry, F. Legendre, T. Leguey, M. Lewandowska, R. Lindau, E. Marquis, A. Muñoz, B. Radiguet, Z. Oksiuta, Review on the EFDA work programme on nano-structured ODS RAF steels, J. Nucl. Mater. 417 (2011) 149–153, https://doi.org/10.1016/j.jnucmat.2010.12.065.
[11] S.J. Zinkle, J.L. Boutard, D.T. Hoelzer, A. Kimura, R. Lindau, G.R. Odette, M. Rieth, L. Tan, H. Tanigawa, Development of next generation tempered and ODS reduced activation ferritic/martensitic steels for fusion energy applications, Nucl. Fusion 57 (2017), https://doi.org/10.1088/1741-4326/57/9/092005.
[12] L.L. Hsiung, M.J. Fluss, S.J. Tumey, B.W. Choi, Y. Serruys, F. Willaime, A. Kimura, Formation mechanism and the role of nanoparticles in Fe-Cr ODS steels developed for radiation tolerance, Phys. Rev. B - Condensed Matter Mater. Phys. 82 (2010) 184103, https://doi.org/10.1103/PHYSREVB.82.184103.
[13] P. Dou, S. Jiang, L. Qiu, A. Kimura, Effects of contents of Al, Zr and Ti on oxide particles in Fe–15Cr–2W–0.35Y2O3 ODS steels, J. Nucl. Mater. 531 (2020), https://doi.org/10.1016/J.JNUCMAT.2020.152025.
[14] H. Xu, W. Li, X. Sha, J. Meng, C. Kang, W. Wang, X. Zang, Z. Wang, Effects of Zr addition on the microstructural stability of 15Cr-ODS steels under elevated-temperature annealing, Fusion Eng. Des. 138 (2019) 231–238, https://doi.org/10.1016/J.FUSENGDES.2018.11.048.
[15] W. Li, H. Xu, X. Sha, J. Meng, Z. Wang, Microstructure and mechanical properties of 14Cr-ODS steels with Zr addition, High Temp. Mater. Processes 38 (2019) 404–410, https://doi.org/10.1515/htmp-2018-0067.

[16] Z. Oksiuta, N.L. Baluc, Role of Cr and Ti contents on the microstructure and mechanical properties of ODS ferritic steels, Adv. Mater. Res. 59 (2009) 308–312, https://doi.org/10.4028/WWW.SCIENTIFIC.NET/AMR.59.308.
[17] L. Zhang, L. Yu, Y. Liu, C. Liu, H. Li, J. Wu, Influence of Zr addition on the microstructures and mechanical properties of 14Cr ODS steels, Mater. Sci. Eng. A 695 (2017) 66–73, https://doi.org/10.1016/J.MSEA.2017.04.020.
[18] Titanium Metal - Historical Statistics (Data Series 140) | U.S. Geological Survey, (n.d.), https://www.usgs.gov/media/files/titanium-metal-historical-statistics-data-series-140.
[19] Zirconium - Historical Statistics (Data Series 140) | U.S. Geological Survey, (n.d.), https://www.usgs.gov/media/files/zirconium-historical-statistics-data-series-140.
[20] N. Liu, X. Cao, T. Zhao, Z.W. Zhang, Progress of zirconium alloying in iron-based alloys and steels, Mater. Sci. Technol. (U. K.) 37 (2021) 830–851, https://doi.org/10.1080/02670836.2021.1958488.
[21] M. Frelek-Kozak, K. Kurpaska, M. Mulewska, R. Zieliński, A. Diduszko, D. Kosińska, W. Kalita, M. Chromiński, K. Turek, A. Kaszyca, J.J. Zaborowska, Mechanical behavior of ion-irradiated ODS RAF steels strengthened with different types of refractory oxides, Appl. Surf. Sci. 610 (2023) 155465, https://doi.org/10.1016/J.APSUSC.2022.155465.
[22] D. Pazos, A. Cintins, V. de Castro, P. Fernández, J. Hoffmann, W.G. Vargas, T. Leguey, J. Purans, A. Anspoks, A. Kuzmin, I. Iturriza, N. Ordás, ODS ferritic steels obtained from gas atomized powders through the STARS processing route: reactive synthesis as an alternative to mechanical alloying, Nucl. Mater. Energy 17 (2018) 1–8, https://doi.org/10.1016/j.nme.2018.06.014.
[23] M. Oñoro, J. Macías-Delgado, M.A. Auger, V. de Castro, T. Leguey, Mechanical properties and stability of precipitates of an ODS steel after thermal cycling and aging, Nucl. Mater. Energy 24 (2020), https://doi.org/10.1016/j.nme.2020.100758.
[24] M. Oñoro, V. de Castro, T. Leguey, J. Pöpperlová, R.M. Huizenga, M.A. Auger, Microstructural stability of secondary phases in an ODS ferritic steel after thermal aging at 873 K, Mater. Charact. 207 (2024), https://doi.org/10.1016/J.MATCHAR.2023.113517.
[25] M. Oñoro, T. Leguey, V. de Castro, M.A. Auger, Effects of thermal aging at 873 K on the impact properties of an ODS ferritic steel, Nucl. Mater. Energy 36 (2023), https://doi.org/10.1016/J.NME.2023.101455.
[26] N. Ordás, E. Gil, A. Cintins, V. de Castro, T. Leguey, I. Iturriza, J. Purans, A. Anspoks, A. Kuzmin, A. Kalinko, The role of yttrium and titanium during the development of ODS ferritic steels obtained through the STARS route: TEM and XAS study, J. Nucl. Mater. 504 (2018) 8–22, https://doi.org/10.1016/j.jnucmat.2018.03.020.
[27] D.A. Venero, M. Oñoro, S. Parnell, SANS study of the nanosized features in oxide dispersion strengthened alloys, ISIS Neutron Muon Source Data J. (n.d.). doi: 10.5286/ISIS.E.RB2310339-1.
[28] SasView for Small Angle Scattering Analysis, n.d., https://www.sasview.org/help/.
[29] J.J. Rehr, R.C. Albers, Theoretical approaches to X-ray absorption fine structure, Rev. Mod. Phys. 72 (2000) 621, https://doi.org/10.1103/RevModPhys.72.621.
[30] B. Ravel, M. Newville, ATHENA, ARTEMIS, HEPHAESTUS: data analysis for X-ray absorption spectroscopy using IFEFFIT, J. Synchrotron Rad. 12 (2005) 537–541, https://doi.org/10.1107/S0909049505012719.
[31] M. Newville, EXAFS analysis using FEFF and FEFFIT, J. Synchrotron Radiat. 8 (2001) 96–100, https://doi.org/10.1107/S0909049500016290.
[32] M. Oñoro, S.R. Parnell, E. Salas-Colera, D. Alba Venero, V. Martin-Diaconesu, T. Leguey, V. de Castro, M.A. Auger, Secondary phases characterization by SANS and XAS of an ODS ferritic steel after thermal aging at 873 K, Nucl. Mater. Energy 39 (2024) 101671, https://doi.org/10.1016/J.NME.2024.101671.
[33] A. Machida, H. Saitoh, T. Hattori, A. Sano-Furukawa, K. Funakoshi, T. Sato, S. Orimo, K. Aoki, Hexagonal close-packed iron hydride behind the conventional phase diagram, Sci. Rep. 9 (2019) 1–9, https://doi.org/10.1038/s41598-019-48817-7.
[34] The International Centre for Diffraction Data - ICDD, (n.d.), https://www.icdd.com/.
[35] A. Guinier, C.B. Walker, N. York, J. Wiley. Small-Angle Scattering of X-rays, Wiley, 1955, https://doi.org/10.1126/science.123.3197.591.c.
[36] A. Jain, P. Shyue, G. Ong, W.C. Hautier, D. William, S. Richards, S. Dacek, D. Cholia, D. Gunter, G. Skinner, K.A. Ceder, S.P. Persson, W.D.R. Ong, The materials project: a materials genome approach to accelerating materials innovation, APL Mater. 17 (2023), https://doi.org/10.1063/1.4812323.